1 **Synthetic sodalite doped with silver nanoparticles:**

2 **Characterization and Mercury (II) removal from aqueous solutions**

3

4 Tauanov, Z.[1,2], Tsakiridis P.E.[3], Shah, D[1] and Inglezakis, V.[1,2*]

5 *[1] Environmental Science and Technology Group (ESTg), Chemical & Materials Engineering*

6 *Department, School of Engineering, Nazarbayev University, Astana, 010000, Kazakhstan.*

7 *[2] The Environment & Resource Efficiency Cluster (EREC), Nazarbayev University, Astana, 010000,*

8 *Kazakhstan.*

9 *[3] School of Mining and Metallurgical Engineering, National Technical University of Athens, Athens,*

10 *Greece.*

11

12 **Abstract**

13 In this work, a novel silver-doped synthetic sodalitic composite was synthesized and characterized

14 using advanced characterization methods, namely TEM-EDS, XRD, SEM, XRF, BET, zeta

15 potential and particle size analysis. The synthesized nanocomposite was used for the removal of

16 Hg^{2+} from 10 ppm aqueous solutions of initial pH equal to 2. The results showed that the sodalitic

17 nanocomposites removed up to 98.65% of Hg^{2+}, which is approximately 16% and 70% higher than

18 the removal achieved by sodalite and parent coal fly ash, respectively. The findings revealed that

19 the Hg^{2+} retention in nanocomposite microstructure is a multifaceted mechanism that predominantly

20 involves adsorption, precipitation and Hg-Ag amalgamation. The study of the anions effect (Cl^-,

21 NO_3^-, $C_2H_3O_2^-$ and SO_4^{2-}) indicated that the Hg^{2+} uptake is comparatively higher when Cl^- anions

22 co-exist with Hg^{2+} in the solution.

23 **Keywords:** Coal fly ash; synthetic sodalite; silver nanoparticles; mercury removal;

24 nanocomposites; water treatment.

25 _____

1   * Address correspondence to Vassilis Inglezakis, 53, Kabanbay batyr Avenue, Astana, Kazakhstan,

2   010000; Phone: +7-7172-706534.

3   Email: vasileios.inglezakis@nu.edu.kz

4   **Introduction**

5   Fly ash-derived porous materials have attracted the interest with recent progress and expanding

6   range of applications, particularly as cost effective and easy-to-process adsorbent for wastewater

7   and gaseous emmisions purification [1–5]. Depending on the reaction conditions, the coal fly ash

8   (CFA) can be converted into useful and stable porous materials, such as zeolites [1,6,7] and sodalites

9   [8,9]. Sodalite belongs to the group of aluminosilicates and is considered as thermodynamically

10 stable among several porous aluminosilicate materials, such as zeolites and geopolymers. Synthetic

11 sodalities can be produced from industrial waste fly ash [10,11] and kaolin [12,13]. There are many

12 applications, where sodalites have been successfully utilized such as catalysts for hydrogenation

13 reaction [14], substrates for a photoluminescence material [15] and hollow mesoporous structure for

14 drug release [16].

15 More recently, sodalities and sodalitic composites that contain metal and metal oxide nanoparticles

16 have attracted considerable interest in the field of wastewater treatment for the removal of inorganic

17 and organic pollutants. Although CFA-derived synthetic and natural zeolites are commonly used for

18 heavy metals and ammonium removal [5,17,18] , there are limited studies on sodalite group of

19 materials. Despite the fact that the sodalite has a low sorption capacity, the size channels and cages

20 of its porous material framework allow a preferential adsorption of relatively small cations, such as

21 Ca^{2+} [19], Ag^+ [20] and Cd^{2+}, Pb^{2+} [21].

22   Amongst several pollutants, mercury, owing to its toxicity, has turned into an pressing

23 environmental problem. Several studies have been conducted on removal of elemental mercury

24 (Hgº) from coal combustion flue gas and Hg^{2+} from water, employing various physical and

25 chemical methods, such as fiber-based and membrane bioreactors [22,23], adsorption, catalytic [24] and

26 thermal [25] methods, wet electrostatic precipitators [26], vacuum ultraviolet light and heat co-

1 activation method [27], and bioremediation [28]. Among these methods the most popular, cost

2 effective, and widely applied is adsorption by use of various porous, non-porous, functionalized and

3 surface modified sorbents. Table 1 summarizes recent studies on waste-derived and natural

4 adsorbents for the removal of Hg^{2+} from water. As could be observed from the Table 1, the waste-

5 derived and natural adsorbents have the adsorption capacity ranging between 0.1 to 41.7 mg/g.

6 While there are several closely related studies on mercury remediation using CFA-based zeolites

7 [1,29], a detailed mechanistic studies and examination on CFA-derived sodalites doped with silver

8 nanoparticles (Ag NPs) for retention of Hg^{2+} from aqueous phase is inadequtly presented, if at all,

9 in the related literature.

10 The present study is a continuation of our research on fly ash-derived adsorbents for the removal of

11 Hg2+. In our previous work[31] analcime (zeolite) nanocomposite was synthesized while in the

12 present work sodalite, which is generally considered a non-zeolitic anhydrous tectosilicate. The

13 materials are markedly different as is evidenced by the different XRD patterns, BET surface areas,

14 zeta potential profiles and Ag content. Herein, we explore the utilization of Ag NPs containing

15 sodalitic nanocomposites for Hg^{2+} removal. Considering a relatively low-cost CFA resource, it

16 could be effectively applied to produce Ag NPs containing composites that may address two issues:

17 effective utilization of waste CFA, and production of a useful adsorption for the treatment of

18 wastewater contaminated with Hg^{2+}. In particular, in this work, CFA derived synthetic sodalites and

19 novel Ag NPs doped porous sodalitic nanocomposites are synthesized and examined for Hg^{2+}

20 removal in batch mode. The obtained sodalite and Ag NPs doped sodalitic nanocomposite are

21 compared with the CFA in terms of microstructure, mineralogy, morphology and removal

22 capacities. Furthermore, four types of Hg^{2+} salts, namely with acetate, sulfate, nitrate and chloride,

23 were used to study the effect of the co-existing anions on the removal of Hg^{2+}. Moreover, a of the

24 removal efficiencies of the materials are discussed in relation to their to physical and chemical

25 properties. Advanced characterization methods were used for the elucidation of possible removal

26 mechanism of mercury.

1

Materials and methods

Materials and synthesis procedure

The CFA samples used in this work were collected from the electrostatic fly ash precipitators of East Kazakhstan power station and labelled as M-CFA (Oskemen, 252 MW). The chemicals used for synthesis were of analytical grade. Sodalites were synthesized *via* a traditional alkaline hydrothermal treatment of fly ash at 110 °C, in a 1-L chemical resistant heavy wall reactor using aqueous solution of 3 M sodium hydroxide (NaOH) (Sigma-Aldrich). The reaction time was set at 48 hours to produce synthetic sodalite (SOD) with substantial yield. The synthesis of sodalite underwent a similar protocol as the synthesis of CFA-derived zeolite produced in our previous work [2,30,31].

The SOD was subsequently enriched with silver nanoparticles (Ag NPs) to produce the nanocomposite used for the removal of mercury. The doping of Ag NPs into microstructure of sodalite was carried out via ion exchange followed by reduction. In the beginning, sodalite samples were left to dry at 300 °C for 3 hours to evaporate water entrapped in the microstructure of material. Then, an adapted silver ion-exchange method [32,33] was carried out by adding 10 mL of 10 mM aqueous solution of silver nitrate ($AgNO_3$, Sigma-Aldrich) per 1 g of sodalite and left to cure for 12 hours. The reaction reservoir was covered with aluminium foil and stored in dark to avoid oxidation of silver ions. Finally, the produced sodalite slurry underwent a drying procedure at 130 °C for consecutive 3 hours. After that, the soaking method by adding 10 mL of 10 mM aqueous solution of $AgNO_3$ was duplicated to obtain intermediate product of silver ion-exchanged sodalites. The latter was subsequently calcined for 3 hours at 500 °C and continued with a 4-hour reduction reaction of silver ions by means of sodium borohydride ($NaBH_4$, Fischer-Scientific) as a reducer, which yielded a silver-doped synthetic sodalitic nanocomposite (Ag-SOD). The same method was conducted without adding $AgNO_3$ solution (ultrapure water was added in the same volume of 10

mL) to sodalite to examine the reduction effect (R-SOD) on sodalite microstructure and compare the removal capacity of produced and parent materials.

Characterization of materials

The elemental analysis of parent M-CFA, SOD and Ag-SOD was conducted on X-Ray fluorescence (XRF, PANalytical). The crystalline phases present in raw and produced materials were studied on X-Ray diffraction (XRD) using a Bruker D8-Focus diffractometer with Ni-filtered CuKα radiation (λ = 1.5406 Å), at 40 kV and 40 mA.

The surface morphology of materials was studied by Scanning Electron Microscopy (SEM) using a JEOL 6380LV Scanning Electron Microscope, operating in LV mode, at 20 kV, equipped with a backscattered electron detector. Spot and area analyses were conducted with a Si (Li) Energy-Dispersive X-ray spectrometer (INCA X-sight, Oxford Instruments), connected to SEM. The nanoscale investigation was achieved with a high resolution JEOL JEM-2100 LaB$_6$ transmission electron microscope (HRTEM), operating at 200 kV. Prior to analysis, the suspension of samples (ca. 0.2 g) were prepared in alcohol solution and cured with ultrasound to disaggregate any agglomerated particles. A drop from the suspension was then placed on a 300-mesh carbon coated copper grid and air-dried overnight. The grain microstructure was also studied using a bright field detector in scanning (STEM) mode. Elemental analysis was performed using an Oxford X-Max 100 Silicon Drift Energy Dispersive X-ray spectrometer (EDS) in connection with TEM, with a probe size ranging from 2 to 5 nm in STEM mode.

The materials porosity was measured on Autosorb-1 nitrogen porosimeter (Quantochrome, UK). The size of pores and total volume of samples were calculated from the results by means of in-built computing method, wherein the specific surface area (SSA) was quantified using the BET model. The particle size distribution (PSD) was analyzed using Particle Size Analyzer (PSA, Malvern Mastersizer 3000) in wet dispersion mode with ultrapure water being used as dispersant. The zeta-

1 potential of materials under various pH values (from pH 2.0 to 12.0) was studied using a Zetasizer

2 (Malvern Zetasizer Nano ZS, UK).

3

4 ***Batch adsorption kinetics***

5 Mercury (II) solution (Hg^{2+}) with a volume of 100 ml and concentration of 10 ppm with an adjusted

6 initial pH value of 2.0 was mixed with 0.75 g of solid samples into a glass container under static

7 conditions and ambient temperature. The pH of solutions was adjusted using concentrated

8 hydrochloric acid (HCl). The selected concentration of Hg^{2+} used in this work is based on literature

9 values [1,29,34,35]. Analytical grade Hg^{2+}chloride and ultrapure water were used for the preparation of

10 solutions . A volume of 0.1-0.2 mL aliquots were collected after selected period of time and

11 analysed for Hg^{2+}. The overall volume of aliquots was up to 2.0 % of the initial solution volume.

12 The residual concentration of mercury was quantified using the mercury analyser RA-915 M

13 (Lumex) with a pyrolysis attachment that can measure total mercury with a detection limit of 1 ppb

14 for a sampe volume of 10-200 μL. Two control solutions were prepared. The first without solid

15 sample to assess the potential adsorption of Hg^{2+} on the container walls and the second with

16 ultrapure water at the same pH to study the leaching of silver ions from the nanocomposites.

17 According to results, the loss of mercury due to adsorption on container walls and/or evaporation

18 are limited to an average of 5.5 %, while the leaching of silver ions from the nanocomposites was

19 less than 0.1 ppm. The adsorption experiments were duplicated with an average standard deviation

20 of 1.3 %.

21

22 ***Effect of the co-existing anions***

23 The co-existing anions effect on the removal of Hg^{2+} from solution using Ag-SOD was examined.

24 Four soluble Hg^{2+}salts were selected, namely chloride ($HgCl_2$); nitrate ($Hg(NO_3)_2$); sulfate ($HgSO_4$)

25 and acetate ($HgAc_2$). The same experimental conditions were applied for all Hg^{2+}salts by adding

26 0.15 g of nanocomposite (Ag-SOD) into 50 mL Hg^{2+} solutions with initial concentration of 10

1 mg/L. The pH value of all Hg^{2+} solutions were adjusted to pH 2.0 using concentrated HCl. The

2 samples were analyzed for residual concentration of Hg^{2+} ions on mercury analyzer RA-915 M

3 using 0.05-0.1 mL of aliquots from adsorption containers after set period of duration: 15, 24 and 48

4 hours. The experiments with all mercury (II) salts were carried out in duplication and static

5 conditions at ambient temperature.

6

Results and discussion

Synthesis and Characterization

9 The elemental composition of M-CFA, synthetic SOD and Ag-SOD are presented in Table 2. M-

10 CFA is primarily comprised of alumina and silica (ca. 66 wt.%) with Si/Al ratio of ~1.06. These

11 findings in connection with a small amount of CaO (ca. 4.53 wt.%), MgO (ca. 1.14 wt.%) and SO_3

12 (ca. 0.69 wt.%) indicate that the coal source used during this CFA production was of bituminous

13 origin, which in turn corresponds to Type F CFA. Fe_2O_3 content of M-CFA is in a relatively high

14 conecntration, reaching 23.1wt.%. On the other hand, both SOD and Ag-SOD contain 6- to 7-fold

15 higher amount of Na_2O compared to parent M-CFA, which is mostly due to the alkaline

16 hydrothermal treatment with NaOH, while the starting K_2O content in M-CFA (~1.86 wt.%) has

17 been reduced, being replaced by sodium ions, reaching on average 0.25 wt.%. The Ag NPs content

18 in Ag-SOD is approximately 2.09 wt.%, which is calculated from the oxide form of silver (Ag_2O)

19 based on XRF results and is close to the theoretical value calculated from material balance

20 (2.15wt.%).

21

22 Figure 1 shows the corresponding XRD patterns of M-CFA, R-SOD, SOD and Ag-SOD. According

23 to spectrums, a considerable quantity of amorphous material was observed in the range of 10º-15º, a

24 characteristic diffused wide band of a glassy phase. The results concludingly indicate that during

25 the hydrothermal treatment of M-CFA that inherently contains the aluminosilicate phases as mullite

26 and quartz, sodalitic phase developed gradually and is observed as the major phase in samples of

SOD and Ag-SOD. Consecutively, the amount of mullite and quartz in produced SOD and Ag-SOD were considerably diminished; primarily because of fractional dissolution and the subsequent sodalite phase progression. The obtained spectrum of the Ag-SOD clearly shows the presence of metallic Ag NPs in the sodalitic matrix, identified by the characteristic peaks at 38.18º, and 44.33º. The SEM analysis of parent M-CFA and produced Ag-SOD also confirms the formation and growth of sodalite crystals on M-CFA particles. The micrographs of M-CFA in Figure 2 shows that it predominantly possess a granular and spherical shape with the size of particles ranging between 5 and 30 μm, while the produced nanocomposite demonstrated a considerably porous "sponge-like" structure.

According to our hypothesis, the inherently containing aluminosilicate and silicate compounds (mullite, amorphous glass and quartz) in M-CFA acted as the substrate for the growth of sodalite crystals and transformed into sodium aluminates and silicates. They facilitated the necessary nucleation sites for sodalite evolution and led to the partial development of porous synthetic sodalite on and inside the M-CFA spheres, with an approximate length of 1-2 μm. The high concentration of Na^+ appears to stabilize the sub-micron building blocks of the forming sodalite crystalline structure. The detection of finer configurations could be related to the presence of insignificant amount of amorphous sodalite formations, during transformation with lower Al content. On the other hand, the presence of Ag NPs in the SOD matrix did not significantly affect their structure. The presence of metallic silver nanoparticles detected by XRD analysis was also confirmed by TEM imaging (Figure 3). Almost no metallic silver agglomeration was observed, indicating a uniform matrix with well dispersed Ag NPs throughout the Ag-SOD. The metallic Ag NPs is observed to be well dispersed in the nanocomposite matrix, with low degree of agglomeration, ranging from 10 to 50 nm. In most cases the particles are well defined and spherical with an average size of 20 nm.

The specific surface area (SSA) results, as shown in Table 3, reveal that the BET surface area of parent M-CFA is the lowest. It is commonly known that synthetic sodalities and zeolites derived from CFAs typically possess SSA that ranges between 8 and 75 m^2/g [9,36,37], that is predominantly mesoporous matrix. The published results are in agreement with data of this work, as the produced SOD has a SSA of 67 m^2/g. The R-SOD has about ~30% lower SSA than SOD, because of the high temperature calcination process during synthesis, which possibly resulted in partial damage of matrix. The Ag-SOD shows a SSA of 51 m^2/g that is similar to R-SOD, but the average pore size and pore volume is significantly lower, indicting partial blockage of the micropores due to Ag NPs doping, as has also been suggested by by Wdowin et al. [38].

Table 4 shows the particle size distribution (PSD) results of parent M-CFA and synthesised materials. The Ag-SOD revealed a relatively smaller particles size than parent M-CFA and SOD. The 90 vol% of the particles of SOD have size lower than 157 μm and 50 vol% of it below 28.5 μm. The corresponding values in Ag-SOD are 57.8 μm and 20.3 μm. The obtained results might be due to the agglomeration and de-agglomeration phenomena of synthetic sodalites fine particles during and after the high temperature calcination. This in turn might have an effect on adsorption kinetics, as the adsorption rate is function of particles size.

Adsorption kinetics

During the kinetics studies pH increased from 2.0 to 3.3 for M-CFA and up to pH 7.0 for SOD and Ag-SOD, whereas the value of conductance decreased from 2680 μS/cm to 980 μS/cm for M-CFA and reached nearly 760 μS/cm for SOD and Ag-SOD. It should be noted that the conductivity and pH evolution was nearly the same for the sodalite control reactors, i.e. SOD in water. Therefore, a decreasing conductance values could be related to the ion exchange between H$^+$ from the solution and Na$^+$ from the surface of solids, which also resulted in pH increase.

The adsorption kinetics results reveal that the Ag-SOD has reached an equilibrium removal of approximately 99% in 24 hours, while it took 12 days and 14 days for SOD and R-SOD to reach

1 82% and 66%, respectively (Figure 4). The divergence in mercury uptake performance indicates a

2 complex removal mechanism in nanocomposite in comparison with SOD and R-SOD materials,

3 since it adsorbs Hg^{2+} in a significantly faster rate. The M-CFA demonstrated a poor adsorption

4 behavior of Hg^{2+} ions, with only 30% removal after 14 days, from water as expected, considering

5 its low BET surface area and less amount of ion-exchangable cations. In summary, both the

6 removal rate and adsorption capacity of Hg^{2+} ions follow theorder: Ag-SOD > SOD > R-SOD >>

7 M-CFA. The order is in agreement with the SSA results of the parent and produced solids, which in

8 turn confirms that the adsorption is the principal mechanism of retention in parent and reference

9 materials (SOD, R-SOD and M-CFA), while the retention of Hg^{2+} ions in nanocomposite (Ag-

10 SOD) considerably differs. The results suggest that the removal mechansism on Ag-SOD is

11 predominantly an amalgamation reaction between Hg and Ag, in parallel to adsorption and surface

12 precipitation.

13 As it is shown in particle size distribution analysis in Table 4, the average size of Ag-SOD is

14 slightly smaller than of the parent SOD, which correspondingly positively affected the adsorption

15 rate. However, despite having the lowest particle size of all samples, the kinetics of R-SOD is much

16 slower in comparison with SOD and Ag-SOD. This proves that the adsorption behavior in these

17 materials is not only governed by the size of particles but other factors contribute too.

18 In addition to BET surface area and size of particles, the oxidation and reduction (redox) potentials

19 of Hg and Ag play a vital role in determining the adsorption behavior. This is particularly important

20 in the case of Ag-SOD where the redox reactions between $Ag°/Ag^+$ (+0.80 V) and $Hg^{2+}/Hg°$ (+0.85

21 V), can take place. The hypothesis herein is that there are three co-existing mechanisms in Ag-SOD

22 retention of Hg^{2+} ions, with amalgamation being the predominant one as demonstrated in adsorption

23 kinetics profile and post-adsorption characterizations on TEM. Firstly, the nanocomposite

24 undergoes an adsorption, then mercury cations (Hg^{2+}) are reduced to form Hg°, which in turn

25 precipitates on the surface of nanocomposite and react with the Ag NPs on the surface of the

26 nanocomposite to form an amalgam (Ag_xHg_y). The Hg^{2+} reduction and formation of an amalgam

were also observed by others, who suggested the following possible reaction mechanism between Hg^{2+} and Ag NPs [39,40]:

$$Ag_m + (m/2)\, Hg^{2+} \rightarrow {}_mAg^+ + (m/2)\, Hg$$

$$Ag_n + Hg^{2+} \rightarrow Ag_{(n-2)}Hg + 2Ag^+$$
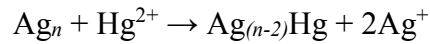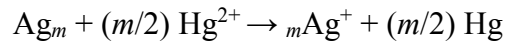
The examination of post-adsorption Ag-SOD samples with adsorbed Hg^{2+} on TEM (Figure 6) confirmed the formation of a new phase Ag/Hg, probably amalgam. It is interesting to note that on mercury-adsorbed Ag-SOD both the amount and size of Ag NPs were significantly reduced to 10-15 nm. Similar results were obtained in our previous work, where CFA-derived synthetic zeolite showed an amalgamation with a very fast and strong adsorption [31]. Another indication that mercury underwent primarily an amalgamation reaction in Ag-SOD matrix is the co-existence of metallic mercury and Ag on the surface as evidenced by EDS-TEM (Figure 6). This confirms the formation of fluids, not dispersed but mainly agglomerated, developing dark long fibrils or non-transmitted large spots on TEM analysis.

It is well known that the surface charge of the solid material could facilitate the adsorption of the oppositely charged species. This could be quantified and examined by determining the zero point charge (pH_{ZPC}) under various pH values, which regulates the electrophoretic mobility where the net charge of the particle is zero. According to the results, the pH_{ZPC} of SOD and Ag-SOD is measured to be around 5.0 (Figure 7). These values show that under strong and medium acidic conditions (until it reaches pH_{ZPC}), both SOD and Ag-SOD have a positive surface charge that should theoretically repeal the positively charged Hg^{2+} ions. However, according to the performance of Ag-SOD the majority of Hg^{2+} ions are removed from solution before reaching pH_{ZPC}, which further supports the proposed hypothesis of amalgam formation in Ag-SOD.

There is an important overlooked aspect in the related literature concerning the speciation of ions in solution, especially in the presence of complexing agents such as Cl^- ions. The speciation of the system was studied by usie of Medusa software and is presented in Figure 8. Evidently, at the pH <

5.0 the predominant species is soluble $HgCl_2$ and therefore, the charge of the nanocomposite surface is not expected to disturb the removal of mercury species in these conditions.

The release of the Ag^+ ions from the nanocomposite Ag-SOD in reference reactors with the same initial pH was negligible (0.8-0.15 ppm). This in turn confirms the virtually complete reduction of initially ion-exchanged Ag^+ into Ag^o on Ag-SOD matrix due to an excess amount of reduction agent ($NaBH_4$) used during the synthesis. Therefore, it can be safely that all the available Ag^o within the matrix of Ag-SOD is reacted with Hg^{2+} to form the amalgam and sample is stable during the whole adsorption experiment. The results allow to conclude that under the studied experimental conditions the mechanism of Ag-SOD is complex and is comprised of primarily amalgamation, physical adsorption and precipitation; whereas the M-CFA, SOD and R-SOD undergo primarily physical adsorption. This, in turn, explains the comparatively fast and efficient removal (up to 99% in 24 hours) of Ag-SOD as compared with SOD and R-SOD.

Effect of the anions on adsorption of Hg^{2+}

With the aim to understand the effect of the anions on adsorption of Hg^{2+} on Ag-SOD, four anions, namely CH_3COO^- (Ac^-), SO_4^{2-}, NO_3^- and Cl^-, were examined (Figure 9). According to the results, Ag-SOD removed up to 99% of Hg^{2+} from the solution in the presence of Cl^-, whereas in the presence of SO_4^{2-} and Ac^- anions the removal was lower at 83.3% and 80.1%, respectively. The lowest removal efficiency was observed for NO_3^- that demonstrated only 70.9% after 48 hours of adsorption. The removal efficiency follows the order: $Cl^- \gg SO_4^{2-} > Ac^- > NO_3^-$. These results show a clear effect of the anions, particularly at the initial steps of adsorption, which could be related to the changes in the speciation of Hg^{2+} and formation of complexes difficult to diffuse into the pore structure of sodalite, affinity Ag-SOD surface and the anion and the size and charge of the anions.

Conclusions

The Hg^{2+} uptake from aqueous solutions, by parent M-CFA, synthetic zeolite SOD and the nanocomposite Ag-SOD has been thoroughly studied. The SOD was found to be the dominant type of porous structure produced from M-CFA. The chemical composition and BET values of the

parent M-CFA and the derived SOD and Ag-SOD are similar to the reported data in the related literature. According to TEM analysis the Ag NPs are spherical with size in the range of 10 and 50 nm. The adsorption kinetics of Hg^{2+} using Ag-SOD demonstrates a very efficient and fast adsorption compared with SOD and M-CFA emphasizing the advantage of doping of parent sodalite with Ag NPs. The analysis of the data indicate that the dominating mechanisms of mercury uptake in SOD and Ag-SOD are different. According to the proposed mechanism, a redox reaction takes place on the surface of the Ag-SOD followed by amalgamation reaction between Hg^o and Ag^o. In addition, the anions effect studies showed that the removal of Hg^{2+} is affected by the presence of different anions and the removal efficiency follows the order $Cl^- \gg SO_4^{2-} > Ac^- > NO_3^-$. The results indicate that CFA-derived synthetic Ag-SOD nanocomposite could effectively be applied for removal of Hg^{2+} ions from water, however further studies are required to study the mechanism of removal and the application of these materials in processes such as fixed beds.

References

[1] Czarna, D.; Baran, P.; Kunecki, P.; Panek, R.; Żmuda, R.; Wdowin, M. Synthetic zeolites as potential sorbents of mercury from wastewater occurring during wet FGD processes of flue gas. J. Clean. Prod. **2018**, *172*, 2636–2645.

[2] Tauanov, Z.; Shah, D.; Itskos, G.; Inglezakis, V. Optimized Production of Coal Fly Ash Derived Synthetic Zeolites for Mercury Removal from Wastewater. IOP Conf. Ser. Mater. Sci. Eng. **2017**, *230*(1).

[3] Jha, B.; Singh, D.N. A three step process for purification of fly ash zeolites by hydrothermal treatment. Appl. Clay Sci. **2014**, *90*, 122–129.

[4] Visa, M.; Chelaru, A.M. Hydrothermally modified fly ash for heavy metals and dyes removal in advanced wastewater treatment. Appl. Surf. Sci. **2014**, *303*, 14–22.

[5] Liu, Y.; Yan, C.; Zhao, J.; Zhang, Z.; Wang, H.; Zhou, S.; Wu, L. Synthesis of zeolite P1 from fly ash under solvent-free conditions for ammonium removal from water. J. Clean. Prod. **2018**, *202*, 11–22.

[6] Zhang, F.-S.; Nriagu, J.O.; Itoh, H. Mercury removal from water using activated carbons derived from organic sewage sludge. Water Res. **2005**, *391. Zhang*(2), 389–395.

[7] Chareonpanich, M.; Jullaphan, O.; Tang, C. Bench-scale synthesis of zeolite A from subbituminous coal ashes with high crystalline silica content. J. Clean. Prod. **2011**, *19*(1), 58–63.

[8] Luo, J.; Zhang, H.; Yang, J. Hydrothermal Synthesis of Sodalite on Alkali-Activated Coal Fly Ash for Removal of Lead Ions. Procedia Environ. Sci. **2016**, *31*, 605–614.

[9] Manique, M.C.; Lacerda, L.V.; Alves, A.K.; Bergmann, C.P. Biodiesel production using coal fly ash-derived sodalite as a heterogeneous catalyst. Fuel **2017**, *190*, 268–273.

[10] Franus, W.; Wdowin, M.; Franus, M. Synthesis and characterization of zeolites prepared from industrial fly ash. Environ. Monit. Assess. **2014**, *186*(9), 5721–5729.

[11] Borhade, A. V.; Kshirsagar, T.A.; Dholi, A.G. Eco-Friendly Synthesis of Aluminosilicate Bromo Sodalite from Waste Coal Fly Ash for the Removal of Copper and Methylene Blue Dye. Arab. J. Sci. Eng. **2017**, *42*(10), 4479–4491.

[12] Maia, A.Á.B.; Neves, R.F.; Angélica, R.S.; Pöllmann, H. Synthesis of sodalite from Brazilian kaolin wastes. Clay Miner. **2015**, *50*, 663–675.

[13] Passos, F.A.C.M.; Castro, D.C.; Ferreira, K.K.; Simões, K.M.A.; Bertolino, L.C.; Barbato, C.N.; Garrido, F.M.S.; Felix, A.A.S.; Silva, F.A.N.G. *In Synthesis and Characterization of Sodalite and Cancrinite from Kaolin BT - Characterization of Minerals, Metals, and Materials 2017*, Springer International Publishing: Cham, 2017.

[14] Liu, F.; Liu, L.-L.; Xue, D.; Li, F.-X. Crystal transformation synthesis, hydrogenation activity and sulfur-tolerant performance of Pt particles encapsulated in sodalite. Ranliao Huaxue Xuebao/Journal Fuel Chem. Technol. **2016**, *44*(4), 477–482.

[15] Kaiheriman, M.; Sidike, A.; Maimaitinasier, A.; Reheman, A.; Rouzi, B. Photoluminescence

properties of Tb3+-doped sodalite under VUV-UV light excitation. J. Lumin. **2015**, *157*, 411–415.

[16] Zuo, S.; Liu, W.; Yao, C.; Li, X.; Luo, S.; Wu, F.; Kong, Y.; Liu, X. One-pot template-free fabrication of hollow mesoporous sodalite nanospheres for drug release. Appl. Clay Sci. **2016**, *119*, 170–174.

[17] Feng, W.; Wan, Z.; Daniels, J.; Li, Z.; Xiao, G.; Yu, J.; Xu, D.; Guo, H.; Zhang, D.; May, E.F.; Li, G. (Kevin). Synthesis of high quality zeolites from coal fly ash: Mobility of hazardous elements and environmental applications. J. Clean. Prod. **2018**, *202*, 390–400.

[18] Pimraksa, K.; Chindaprasirt, P.; Huanjit, T.; Tang, C.; Sato, T. Cement mortars hybridized with zeolite and zeolite-like materials made of lignite bottom ash for heavy metal encapsulation. J. Clean. Prod. **2013**, *41*, 31–41.

[19] Heiden, F.; Nielsen, U.G.; Warner, T.E. Synthesis and thermal stability of the sodalite Na6Zn2[Al6Si6O24](SO4)2 and its reaction with hydrogen. Microporous Mesoporous Mater. **2012**, *161*, 91–97.

[20] Fonseca, A.M.; Neves, I.C. Study of silver species stabilized in different microporous zeolites. Microporous Mesoporous Mater. **2013**, *181*, 83–87.

[21] Eiden-Assmann, S. New heavy metal-hydro-sodalites containing Cd2+, Ag+ or Pb2+: synthesis by ion-exchange and characterisation. Mater. Res. Bull. **2002**, *37*(5), 875–889.

[22] Kozliak, E.I.; Sternberg, S.R.K.; Jacobson, M.L.; Kuether, K.W.; Mann, M.D. Mercury removal from air by a Fiber-Based Bioreactor. Bioremediat. J. **1999**, *3*(4), 291–298.

[23] Huang, Z.; Wei, Z.; Xiao, X.; Tang, M.; Li, B.; Zhang, X. Nitrification/denitrification shaped the mercury-oxidizing microbial community for simultaneous Hg0 and NO removal. Bioresour. Technol. **2019**, *274*(September 2018), 18–24.

[24] Yang, B.; Li, Z.; Huang, Q.; Chen, M.; Xu, L.; Shen, Y.; Zhu, S. Synergetic removal of elemental mercury and NO over TiCe0.25Sn0.25Ox catalysts from flue gas: Performance and mechanism study. Chem. Eng. J. **2018**, *360*(219), 990–1002.

[25] Sotiropoulou, R.E.P.; Serafidou, M.; Skodras, G. Thermal mercury removal from coals: Effect of pyrolysis conditions and kinetic analysis. Fuel **2019**, *238*(June 2018), 44–50.

[26] Duta, A.; Visa, M. Simultaneous removal of two industrial dyes by adsorption and photocatalysis on a fly-ash-TiO2 composite. J. Photochem. Photobiol. A Chem. **2015**, *306*, 21–30.

[27] Kaiheriman, M.; Sidike, A.; Maimaitinasier, A.; Reheman, A.; Rouzi, B. Photoluminescence

1   properties of Tb3+-doped sodalite under VUV-UV light excitation. J. Lumin. **2015**, *157*, 411–415.

2   [28] Wang, X.; He, Z.; Luo, H.; Zhang, M.; Zhang, D.; Pan, X.; Gadd, G.M. Multiple-pathway

3   remediation of mercury contamination by a versatile selenite-reducing bacterium. Sci. Total

4   Environ. **2018**, *615*, 615–623.

5   [29] Attari, M.; Bukhari, S.S.; Kazemian, H.; Rohani, S. A low-cost adsorbent from coal fly ash for

6   mercury removal from industrial wastewater. J. Environ. Chem. Eng. **2017**, *5*(1), 391–399.

7   [30] Tauanov, Z.; Shah, D.; Inglezakis, V.; Jamwal, P.K. Hydrothermal synthesis of zeolite

8   production from coal fly ash: A heuristic approach and its optimization for system identification of

9   conversion. J. Clean. Prod. **2018**, *182*, 616–623.

10   [31] Tauanov, Z.; Tsakiridis, P.E.; Mikhalovsky, S.V.; Inglezakis, V.J. Synthetic coal fly ash-

11   derived zeolites doped with silver nanoparticles for mercury (II) removal from water. J. Environ.

12   Manage. **2018**, *224*(July), 164–171.

13   [32] Golubeva, O.Y.; Ternovaya, N.Y.; Mal'tseva, N. V.; Meyerstein, D. Catalytic hydrogen

14   oxidation using zeolite RHO modified by silver nanoparticles. Glas. Phys. Chem. **2012**, *38*(5), 455–

15   459.

16   [33] Golubeva, O.Y.; Ul'yanova, N.Y.; Kurilenko, L.N. Synthesis and study of catalytic activity of

17   zeolite Rho with varying content of silver nanoparticles. Glas. Phys. Chem. **2013**, *39*(6), 649–653.

18   [34] Sumesh, E.; Bootharaju, M.S.; Anshup; Pradeep, T. A practical silver nanoparticle-based

19   adsorbent for the removal of Hg2+ from water. J. Hazard. Mater. **2011**, *189*(1–2), 450–457.

20   [35] Abbas, K.; Znad, H.; Awual, M.R. A ligand anchored conjugate adsorbent for effective

21   mercury(II) detection and removal from aqueous media. Chem. Eng. J. **2018**, *334*(October 2017),

22   432–443.

23   [36] Zeng, S.; Wang, R.; Zhang, Z.; Qiu, S. Solventless green synthesis of sodalite zeolite using

24   diatomite as silica source by a microwave heating technique. Inorg. Chem. Commun. **2016**, *70*,

25   168–171.

26   [37] Li, J.; Zeng, X.; Yang, X.; Wang, C.; Luo, X. Synthesis of pure sodalite with wool ball

27   morphology from alkali fusion kaolin. Mater. Lett. **2015**, *161*, 157–159.

28   [38] Wdowin, M.; Wiatros-Motyka, M.M.; Panek, R.; Stevens, L.A.; Franus, W.; Snape, C.E.

29   Experimental study of mercury removal from exhaust gases. Fuel **2014**, *128*, 451–457.

30   [39] Henglein, A.; Brancewicz, C. Absorption spectra and reactions of colloidal bimetallic

nanoparticles containing mercury. Chem. Mater. **1997**, *4756*(9), 2164–2167.

[40] Henglein, A. Colloidal silver nanoparticles: photochemical preparation and interaction with O2, CCl4, and some metal ions. Chem. Mater. **1998**, *2*(10), 444–450.

[41] Goel, J.; Kadirvelu, K.; Rajagopal, C. Mercury (II) removal from water by coconut shell based activated carbon: Batch and column studies. Environ. Technol. (United Kingdom) **2004**, *25*(2), 141–153.

[42] Mora Alvarez, N.M.; Pastrana, J.M.; Lagos, Y.; Lozada, J.J. Evaluation of mercury (Hg2+) adsorption capacity using exhausted coffee waste. Sustain. Chem. Pharm. **2018**, *10*(June), 60–70.

[43] Imla Syafiqah, M.S.; Yussof, H.W. Kinetics, isotherms, and thermodynamic studies on the adsorption of mercury (ii) ion from aqueous solution using modified palm oil fuel ash. Mater. Today Proc. **2018**, *5*(10), 21690–21697.

[44] Şahan, T.; Erol, F.; Yılmaz, Ş. Mercury(II) adsorption by a novel adsorbent mercapto-modified bentonite using ICP-OES and use of response surface methodology for optimization. Microchem. J. **2018**, *138*, 360–368.

1

2

FIGURE CAPTIONS

4

Figure. 1. XRD spectra of SOD, R-SOD and Ag-SOD

Figure. 2. SEM images of the Ag-SOD and M-CFA

Figure. 3. TEM images of Ag-SOD

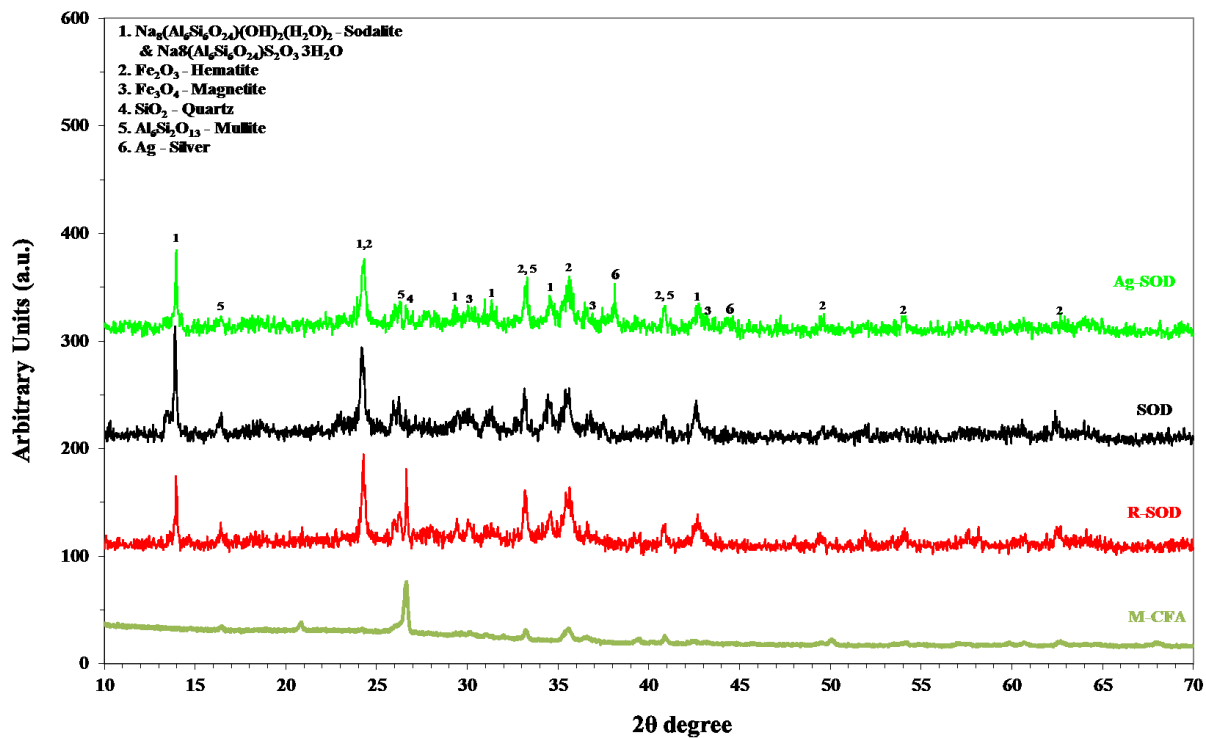**Figure. 4.** Adsorption kinetics of Hg^{2+} in simulated water

Figure. 5. TEM images of Ag-SOD sample loaded with Hg^{2+}

Figure. 6. TEM-EDS analysis of Ag-SOD sample loaded with Hg^{2+}

Figure. 7. Zeta potential values (mV) at different pH: SOD (A) and Ag-SOD (B)

Figure. 8. Speciation of 10 ppm Hg^{2+} solution (0.05 mmol Hg^{2+}, 0.1 mmol Cl^-) [Diagram created
on Medusa software]

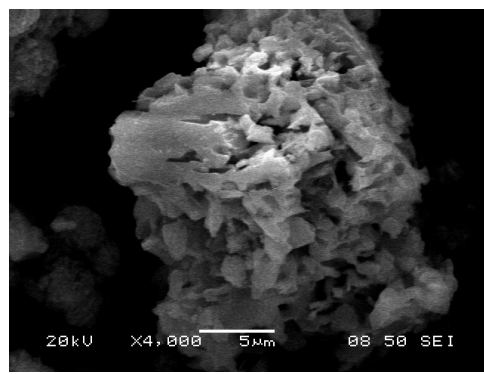**Figure. 9.** Effect of the anions nature on removal of Hg^{2+} from water

15

16

17
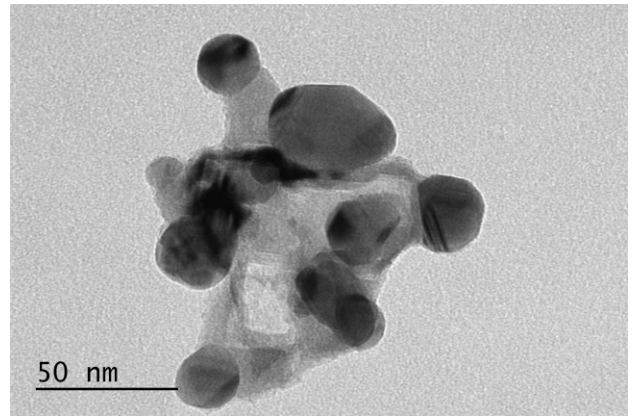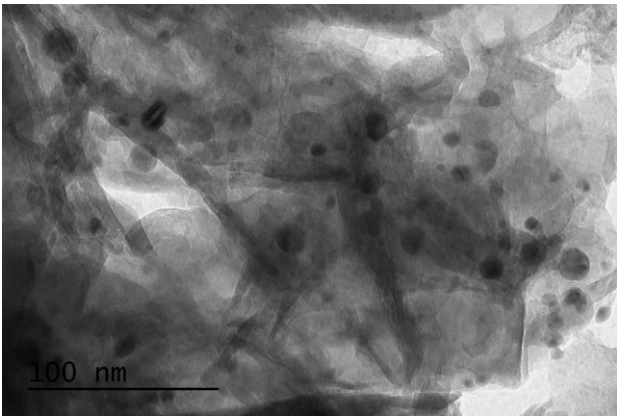
18

19

1. $Na_8(Al_6Si_6O_{24})(OH)_2(H_2O)_2$ – Sodalite
   & $Na8(Al_6Si_6O_{24})S_2O_3\ 3H_2O$
2. Fe_2O_3 – Hematite
3. Fe_3O_4 – Magnetite
4. SiO_2 – Quartz
5. $Al_6Si_2O_{13}$ – Mullite
6. Ag – Silver
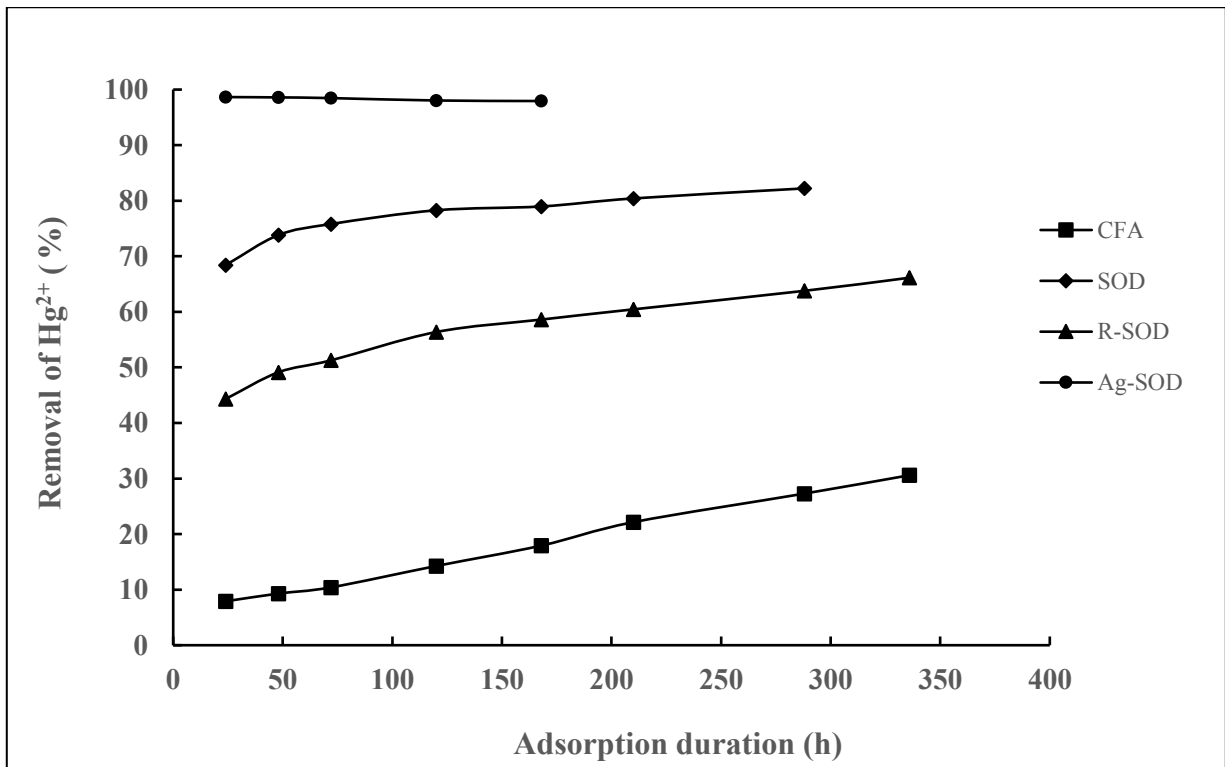
Ag-SOD

SOD

R-SOD

M-CFA
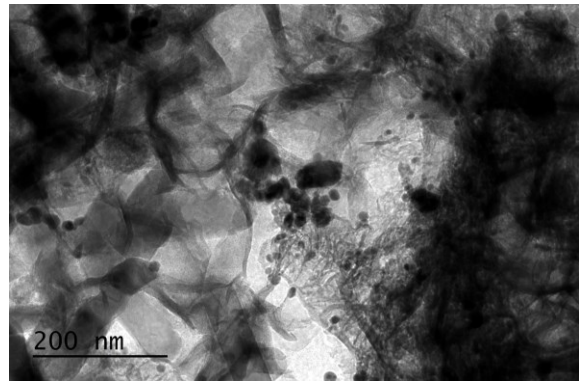
1

Fig. 1

2
3
4
5
6
7

CFA

Ag-SOD
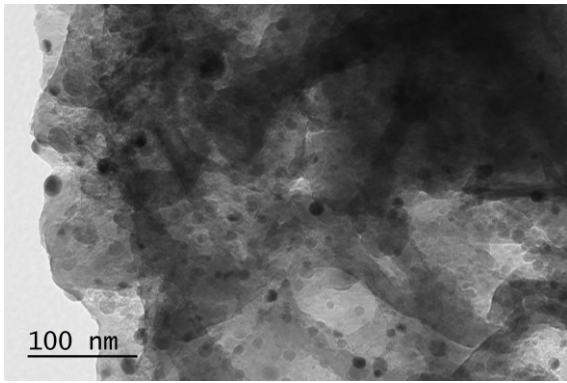
8
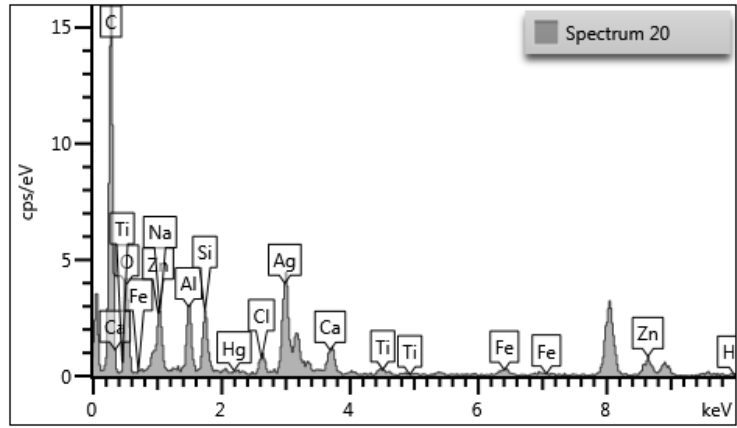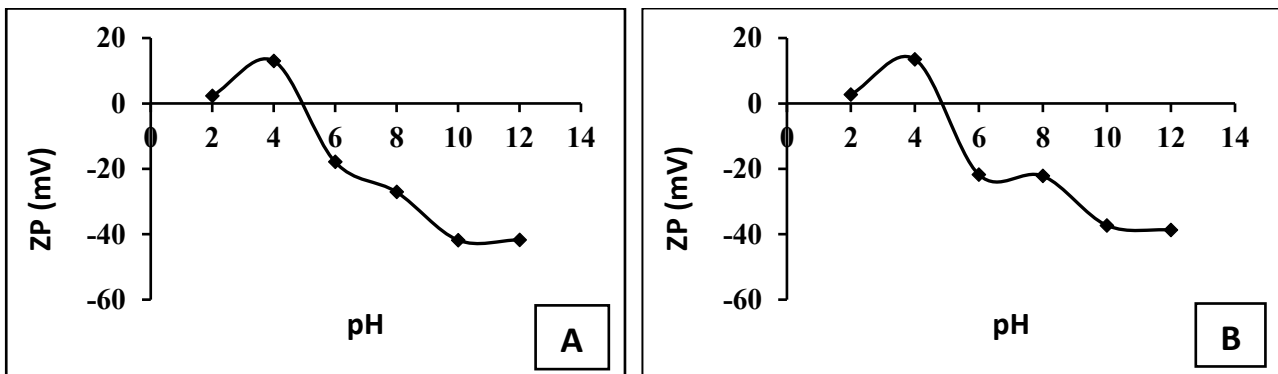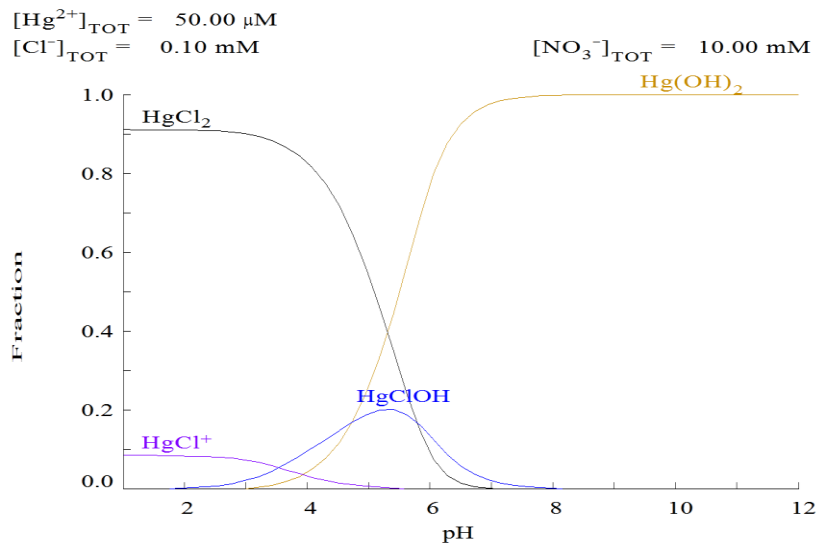9   Fig. 2
10
11
12

1
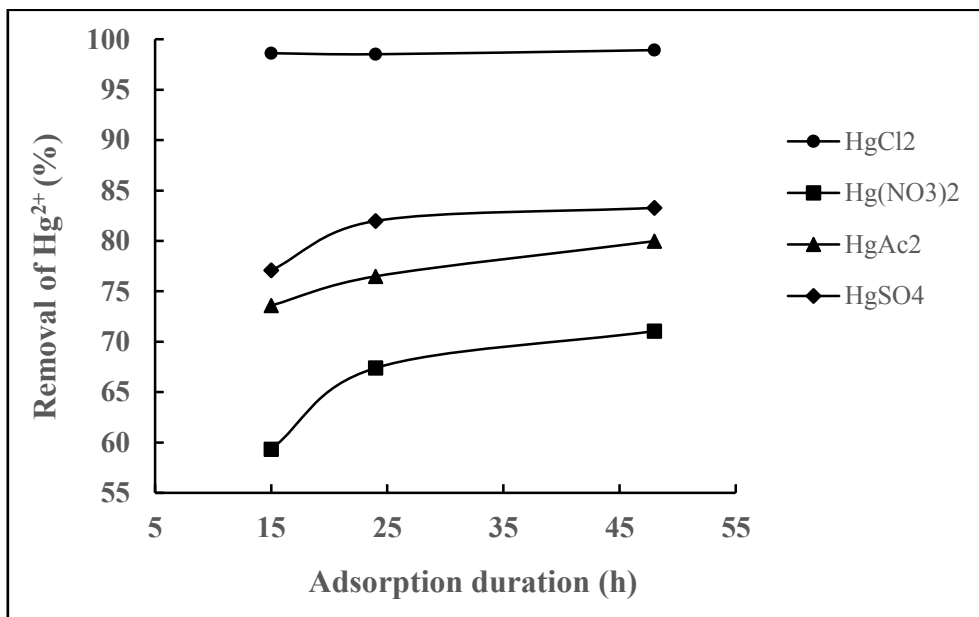2   Fig. 3

3

4

5

6   Fig. 4

1
2   Fig. 5

3

4

5

6

7   Fig. 6

8

9

10

11   Fig. 7

$[Hg^{2+}]_{TOT} = 50.00 \ \mu M$
$[Cl^-]_{TOT} = 0.10 \ mM$
$[NO_3^-]_{TOT} = 10.00 \ mM$

1

2   Fig. 8

3

4

5

6   Fig. 9

7

8

9

10

11

1   **TABLES**

2   **Table 1.** Adsorbents for the removal of Hg^{2+} from water

3   **Table 2.** The elemental composition raw and produced materials (wt.%)

4   **Table 3.** Porosimetric analysis of parent and produced materials

5   **Table 4.** Size distribution results of materials

6

7

8   **Table 1.**

Adsorbent type	Adsorption capacity [mg/g]	Surface area [m²/g]	References
Coconut shell based activated carbon	15.2	1000	[41]
CFA derived Ag NPs doped nanocomposite	6.0	105.0	[31]
Exhausted coffee waste	31.7	11.5	[42]
Modified palm oil fuel ash	1.2	28.5	[43]
Mercapto-modified bentonite	19.3	92.0	[44]
Ag-X CFA derived zeolite	5.0	203	[1]
Linde Type A CFA derived zeolite	0.31	-	[29]

9

10

11

12

13

14

15

16

17

Table 2.

Compound	Ag-SOD	SOD	M-CFA
Na_2O	4.796	5.858	0.763
MgO	1.139	1.145	1.423
Al_2O_3	25.882	24.859	21.750
SiO_2	31.099	32.343	44.425
SO_3	0.696	0.874	2.248
K_2O	0.234	0.260	1.857
CaO	4.533	4.696	6.775
TiO_2	0.939	0.959	1.169
Cr_2O_3	3.460	3.387	0.024
MnO	0.574	0.608	0.432
Fe_2O_3	23.105	23.578	18.138
Co_3O_4	0.088	0.070	0
NiO	0.475	0.477	0.023
CuO	0.046	0.034	0.035
ZnO	0.027	0.036	0.024
SrO	0.286	0.309	0.342
Y_2O_3	0.010	0.009	0.008
ZrO_2	0.092	0.051	0
Ag_2O	2.252	0	0
BaO	0.248	0.273	0.369
CeO_2	0.012	0.151	0.137
P_2O_5	0	0	0.0280
Cl	0	0.023	0.021

Table 3.

Material type	BET surface area, m^2/g	Average pore size, nm	Total pore volume, cm^3/g
M-CFA	20 ± 7.0	15 ± 4.0	0.07 ± 0.05
SOD	67 ± 12	17 ± 3.0	0.26 ± 0.08
R-SOD	47 ± 3.0	16 ± 4.0	0.27 ± 0.12
Ag-SOD	51 ± 1.0	10 ± 0.1	0.13 ± 0.05

Table 4.

PSD	M-CFA	SOD	R-SOD	Ag-SOD
Dv(10), μm	9.7 ± 0.60	8.7 ± 0.42	2.55 ± 0.24	4.4 ± 0.15
Dv(50), μm	67.2 ± 6.40	28.5 ± 0.06	14.14 ± 0.96	20.2 ± 0.70
Dv(90), μm	428 ± 80.0	157 ± 24	48.36 ± 0.57	57.8 ± 0.07